Food Structure 47 (2026) 100511

Contents lists available at ScienceDirect

Food Structure

journal homepage: www.elsevier.com/locate/foostr

Elucidating protein–lipid microstructure and interactions in hybrid processed cheeses using synchrotron macro ATR-FTIR microspectroscopy

Di Lu [a], Jitraporn Vongsvivut [b], Annaleise R. Klein [b], Cushla McGoverin [c,d], Mark Waterland [e], Yi Zheng [f], Alejandra Acevedo–Fani [a], Debashree Roy [a], Harjinder Singh [a], Aiqian Ye [a,*]

[a] Riddet Institute, Massey University, Private Bag 11 222, Palmerston North 4442, New Zealand
[b] Infrared Microspectroscopy (IRM) Beamline, Australian Synchrotron, Australian Nuclear Science and Technology Organisation, 800 Blackburn Road, Clayton 3168, Australia
[c] Dodd–Walls Centre for Photonic and Quantum Technologies, Auckland 1010, New Zealand
[d] School of Food Technology and Natural Sciences, Massey University, Private Bag 11 222, Palmerston North 4442, New Zealand
[e] Department of Physics, University of Auckland, Auckland 1010, New Zealand
[f] AgResearch Group, Bioeconomy Science Institute, Te Rourou, Massey University, Palmerston North 4442, New Zealand

ARTICLE INFO

Keywords:
FTIR microspectroscopy
Synchrotron infrared
Plant protein
Milk protein
Hybrid cheese
Secondary protein structure

ABSTRACT

Herein, synchrotron-based Fourier-transform infrared (S-FTIR) microspectroscopy was used to investigate the spatial distribution and molecular interactions within hybrid processed cheeses (HPCs) that contain casein and plant proteins. Unsupervised hierarchical cluster analysis (HCA) and k-means clustering provided consistent spatial differentiation, effectively separating the regions that were dominated by plant protein from those dominated by casein. Spectral analysis revealed protein–protein and protein–lipid interactions based on the type of plant protein used across plant-based cheeses and hybrid formulations. Cheese samples that contained only hemp protein isolate (HPI) were dominated by β-sheets (50%) and β-turns (21%), while mung bean protein isolate (MPI)-based cheeses exhibited considerable α-helix (35%) and β-sheet (48%) contents. In HPI–casein hybrid cheeses, hydrogen bonds predominated, with the amide II mode of proteins as the key discriminating component. By contrast, the amide I secondary protein structure was the primary marker that distinguished MPI from casein in MPI–casein cheeses. Increasing the casein content reduced plant protein aggregation and created a more heterogeneous environment, thereby supporting a flexible and disordered protein network. Furthermore, the S-FTIR map of lipids indicated that coconut oil was preferentially associated with casein rather than with plant proteins. Overall, these results highlight the role of S-FTIR microspectroscopy in resolving compositional and molecular-level interactions in hybrid cheese matrices.

1. Introduction

Hybrid processed cheese (HPCs), produced by partially replacing milk proteins with plant proteins, are emerging as more sustainable alternatives to conventional cheeses (Zhang et al., 2024). However, incorporating plant proteins, such as hemp protein isolate (HPI) and mung bean protein isolate (MPI), can alter their rheology, texture, functionality, and sensory (Lu, Roy, et al., 2026; Lu et al., 2025). Fundamentally, incorporating plant proteins introduces new molecular and microstructural challenges. In our previous study, we used confocal Raman microscopy to map the distribution of the main components in HPCs formulated with rennet casein (RC) and either MPI or HPI, clearly distinguishing between the dairy and plant protein networks. This analysis revealed complex microstructural segregation and notable molecular changes, showing that the presence of casein altered the secondary structure and tyrosine environment of plant proteins, while the inclusion of plant protein disrupted casein–casein interactions (Lu, McGoverin, et al., 2026). These findings suggest that the internal organisation of HPCs is heterogeneous, and this molecular complexity highlights the need for complementary spectroscopic approaches with higher spatial and structural sensitivity to verify the molecular organisation within such complex matrices.

Fourier-transform infrared (FTIR) spectroscopy has emerged as a powerful analytical tool for probing the molecular composition and

* Corresponding author.
E-mail address: a.m.ye@massey.ac.nz (A. Ye).

https://doi.org/10.1016/j.foostr.2026.100511
Received 18 December 2025; Received in revised form 15 February 2026; Accepted 5 March 2026
Available online 7 March 2026

structure of materials. By measuring the absorption of infrared (IR) radiation, the technique can provide detailed information on functional groups and intermolecular interactions (Jurowski et al., 2024). In particular, vibrational absorption spectra in the mid-IR spectral range (4000–400 cm^{-1}) contain characteristic fingerprints of the key biomacromolecules that serve as the fundamental building blocks of food systems (i.e. proteins, lipids, carbohydrates, and water), making it useful for both qualitative and quantitative analysis of food items (Saji et al., 2024). Furthermore, FTIR microspectroscopy, when combined with a microscope, enables spatially resolved chemical imaging at micron scales, and can be used in combination with multivariate analysis as a label-free, non-destructive tool for characterising complex biological and food systems (Saji et al., 2024).

The development of synchrotron-based FTIR microspectroscopy has considerably advanced these capabilities. Unlike an internal IR source (Globar™) used in most laboratory-based FTIR instruments, the synchrotron-IR source provides a highly collimated and intense IR radiation that substantially enhances spatial resolution and signal-to-noise ratio, enabling the acquisition of high-quality spectra in much shorter scanning times. A macro ATR-FTIR microspectroscopy platform has been developed at the Australian Synchrotron, in which the synchrotron-IR beam is coupled with a high-index germanium (Ge) ATR hemispherical crystal (nGe = 4.0). This optical configuration allows the acquisition of FTIR chemical maps at a resolution four times higher than that of standard transmission and reflectance setups. It allows for a step interval (pixel resolution) of as less as 250 nm, making it ideal for resolving microstructures in complex heterogeneous systems at a few microns, such as single cells and biological tissues (Vongsvivut et al., 2019), as well as drug and nutrient microcapsules (REFs), among others (Kim et al., 2023; Silva et al., 2021; Timilsena et al., 2019).

FTIR techniques have been increasingly applied to cheese and dairy products to monitor their composition, microstructure and structural changes during processing and ripening. For example, FTIR has been used to quantify the key compositions of cheese, such as lipid, protein, salt and moisture contents (Koca et al., 2007; Margolies & Barbano, 2018), and to visualise the spatial distribution of lipid and protein microstructures within cheese matrices (Pax et al., 2019). At molecular level, FTIR combined with Raman microspectroscopy enables the assessment of the secondary structure of proteins by tracking changes in the amide I (ν(C═O) stretching mode of protein backbone) and amide II (mainly δ(N–H) bending and ν(C–N) stretching) regions that reflect maturation processes in cheddar cheese (Dewantier et al., 2023). Recent studies have further integrated FTIR imaging techniques with multivariate analysis to correlate structural changes with functional properties. For example, Ong et al. (2020) demonstrated that pH-dependent alterations in the secondary structure of proteins and microstructural organisation influence the textural properties of cream cheese. Their study reported that low pH conditions were associated with higher β-sheet aggregation, a denser protein matrix and a firmer texture. Furthermore, Pax et al. (2023) showed that synchrotron macro ATR-FTIR microspectroscopy could monitor structural changes in the secondary structure of proteins and alterations in the chemical distribution within mozzarella cheese during freezing and tempering, which could directly affect the performance of thawed cheese. Despite these advances, most FTIR applications have focused on conventional dairy cheeses. More recently, Yiu et al. (2026) used S-FTIR imaging to map structural changes in a pea-protein cheese analogue, showing improved meltability and texture with a dual-polysaccharide system. To date, no studies have reported such advanced analysis of HPCs containing both dairy and plant proteins, leaving a gap for understanding the way mixed-protein systems affect cheese structure and functionality.

Herein, synchrotron macro ATR-FTIR microspectroscopy was used to analyse HPCs formulated with RC and either MPI or HPI, using the same formulations that were previously examined by confocal Raman microspectroscopy (Lu, McGoverin, et al., 2026). The objectives of this study were (i) to map the spatial distribution of lipid, protein and water in single-protein cheese systems, (ii) to distinguish plant proteins from milk proteins in dual-protein systems (plant protein: casein = 50:50) using unsupervised multivariate analysis, (iii) to investigate protein–-protein and protein–lipid interactions within HPCs and (iv) to correlate these observations with our previous Raman microscopy findings to highlight complementary molecular insights between the two techniques. By integrating the synchrotron macro ATR-FTIR technique with multivariate analysis, this study provided an enhanced understanding of the molecular organisation and interactions of plant and dairy proteins in hybrid cheese matrices.

2. Materials and methods

2.1. Materials

RC (SureProteinTM 779) containing 82% protein was obtained from Fonterra Co-operative Group Ltd. (New Zealand). MPI; 85%) was purchased from Bulk Powders New Zealand. HPI; 70%) and virgin coconut oil were purchased from Davis Trading Company (New Zealand). All chemicals used were of analytical grade and were obtained from Sigma Chemical Co., unless otherwise specified.

2.2. Preparation of HPCs

HPCs were prepared by mixing MPI or HPI with RC at ratios of 100:0, 50:50 and 0:100 to obtain a total protein content of 18% (wet weight). The formulation, based on the study by Lu et al. (2025), comprised 18% protein, 20% coconut oil, 0.5% sodium chloride, 0.5% calcium sulfate, 0.1% potassium sorbate, 2.8% trisodium citrate and water on a weight ratio basis, with pH adjusted to ~5.4 using citric acid. HPCs were prepared using a Rapid Visco Analyser (RVA-4; Newport Scientific Pty Ltd, Warriewood, NSW, Australia). The HPC samples (30 g) were prepared in an aluminium cell fitted with a polycarbonate paddle. All dry ingredients and coconut oil were manually blended with water for 5 min and then hydrated in an aluminium cell for 1 h at room temperature (20 °C). The mixture was processed using the following RVA profile: equilibration at 50 °C, heating to 90 °C for 4 min and holding at 90 °C for 10 min. Thereafter, the sample was cooled to 50 °C at a rate of 0.2 °C/s while mixing at 300 rpm throughout the heating and cooling stages. The resulting samples were labelled as MPI100, MPI50, HPI100, HPI50 and RC100, with the numbers indicating the protein ratios within them. Individually packed samples were stored at 4 °C and analysed using synchrotron macro ATR-FTIR microspectroscopy within 1 week.

2.3. Synchrotron macro ATR-FTIR microspectroscopic measurements

Synchrotron FTIR (S-FTIR) microspectroscopic analysis was performed at the infrared microspectroscopy (IRM) beamline of the Australian Synchrotron using a Bruker Vertex V80v spectrometer coupled with a Hyperion 3000 FTIR microscope (Bruker Optik GmbH, Ettlingen, Germany), which was equipped with a liquid nitrogen–cooled narrow-band MCT detector. Spatially resolved chemical mapping was performed using a custom macro-attenuated total reflection (macro ATR) device fitted with a 250-μm diameter facet Ge ATR crystal, as previously described (Ong et al., 2020; Pax et al., 2019; Vongsvivut et al., 2019). Spectra were acquired in the 3800–700-cm^{-1} range at 4 cm^{-1} resolution using the OPUS 8.0 software (Bruker). A background spectrum was first recorded in air (128 co-added scans).

The cheese samples were sliced into ~1–2-mm thickness and pressed against the Ge ATR crystal. The contact quality was monitored via live ATR-FTIR absorbance spectra, with light pressure adjustments as needed. Once good contact with the crystal was established, high-resolution ATR-FTIR maps were collected over areas measuring 90 × 90 μm^2 with a step size of 2 μm. Each spectrum was acquired with 16 co-added scans using a beam-defining projected aperture with a diameter of ~3.1 μm. The default acquisition parameters included three-

term Blackman–Harris apodisation, power spectrum phase correction and a zero-filling factor of 2. Atmospheric compensation was applied to every spectral map using the OPUS 8.0 software suite (Bruker) to remove the effects of atmospheric water vapour and carbon dioxide from the spectra. Each formulation was imaged in duplicate.

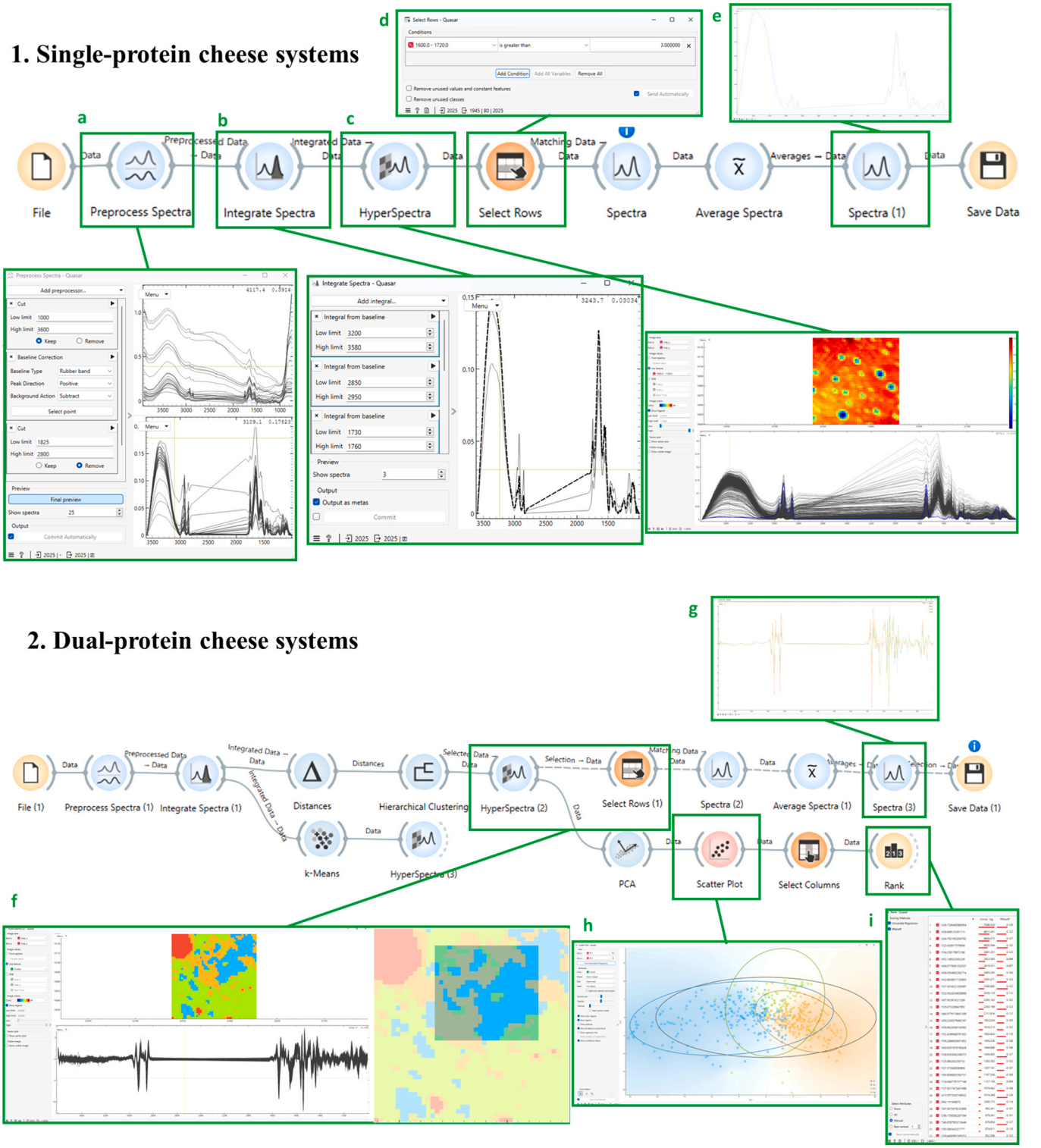

Fig. 1. Workflow for S-FTIR map image data processing in Quasar, including single-protein (top) and dual-protein cheese systems (bottom). The pre–processed data with baseline correction retained spectra in the ranges of 3600–2800 and 1825–1000 cm^{-1} (Box a). Integrated peak mapping was performed using specific spectral regions (Box b), and hyperspectral images were generated after integration (Box c). Spectra were selected based on defined value conditions (Box d), and their average spectra were calculated (Box e). Hierarchical clustering was applied to group the spectra, and the corresponding hyperspectral images were generated after clustering (Box f), and the average spectra of selected regions were extracted (Box g). A scatter plot visualizing cluster separation was obtained after Principal Component Analysis (PCA) (Box h). PC2 was applied to rank protein-related variance (Box i).

2.4. Synchrotron FTIR analysis using Quasar

The spectral data were analysed using Quasar, an open-source Python library designed for machine learning and spectral data visualisation (Toplak et al., 2021). A representative workflow with examples of the single-protein cheese systems (RC100, MPI100 and HPI100) and the dual-protein cheese systems (MPI50 and HPI50) is shown in Fig. 1.

For the single-protein cheese systems, the raw data were preprocessed via a rubber-band baseline correction method, retaining the spectra in the ranges of 3600–2800 and 1825–1000 cm^{-1} (Fig. 1 box a). Chemical maps were generated by integrating areas under the peaks within specific spectral regions to visualise the spatial distribution of the key chemical components: 3580–3200 (water), 2950–2850 and 1760–1730 (lipids), 1700–1600 (amide I) and 1580–1500 cm^{-1} (amide II) for protein and peptide structures (Fig. 1 box b and c). By filtering the rows for specific integrated peaks that meet defined value conditions, group spectra could be selected (Fig. 1 box d) and averaged (Fig. 1 box e) for further comparison and analysis.

For the dual-protein cheese systems, the raw data were preprocessed via rubber-band baseline correction method, second derivatisation with the Savitzky–Golay algorithm (polynomial order 3 and 13 smoothing points) and normalisation via standard normal variate to enhance spectral quality, retaining the spectra in the ranges of 3600–2800 and 1825–1000 cm^{-1}. In addition, two unsupervised clustering algorithms, namely, hierarchical clustering and k-means clustering, were employed to distinguish proteins in the mixed systems. Hierarchical cluster analysis (HCA) was performed using an agglomerative approach, which iteratively grouped similar data points to generate a dendrogram. The Pearson distance was used as the distance measure, with a maximum depth of 10. By contrast, k-means clustering was used to partition the data into a predefined number of clusters, with the cluster centroids iteratively adjusted until convergence. Based on the known composition of the cheese samples and after initial clustering and adjustment, four to five clusters were used to efficiently differentiate lipid and protein types. However, we observed that the two corners (top left and bottom right) of the 90 × 90-μm^2 area lay outside the focused synchrotron-IR beam. To reduce noise, only a small, well-focused central area was selected for detailed analysis (Fig. 1 box f). The average spectra from the selected area were extracted, and principal component analysis (PCA) was conducted to reduce dimensionality and visualise cluster separation through scatter plots (Fig. 1 box h). The second principal component (PC2) was used to rank the variance associated with proteins. Wavenumbers were ranked based on the absolute values of their regression coefficients, highlighting the spectral regions that were highly associated with protein differentiation in the absence of class labels (Fig. 1 box i).

2.5. Deconvolution of the amide I region

The amide I region (1700–1600 cm^{-1}) was deconvoluted for quantitative analysis. First, the average spectrum from the protein-rich cluster, identified using k-means clustering, was extracted from Quasar. Thereafter, the spectra were baseline-corrected using a linear method between two selected points corresponding to the lowest-intensity regions in each spectrum and smoothed using a 5-point Savitzky–Golay filter with a polynomial order of 2 in the Origin® software (2021b) to enhance the signal-to-noise ratio. Subsequently, peak fitting was performed using the second derivative method, followed by an iterative Gaussian peak fitting. Peak assignment was performed using known infrared spectral data for protein secondary structures (Fellows et al., 2020; Sadat & Joye, 2020; Tang et al., 2023). Several iterations were performed until the fit converged, ensuring a final fitting curve with a corrected $R^2 \geq 0.99$. Subsequently, the area under each peak was calculated relative to the total area and expressed in percentage. The results were reported as mean values (performed in triplicate) and standard deviations. The data were subjected to one-way ANOVA analysis using SPSS, followed by Tukey's comparison test. Differences were considered statistically significant at a level of $p < 0.05$. The reported values for β-sheets and β-turns represented the cumulative contributions of multiple peaks.

3. Results and discussion

3.1. Overview of the FTIR spectra of HPCs components

HPCs demonstrated characteristic absorption peaks in the synchrotron ATR-FTIR spectrum, typically within the range of 4000–1000 cm^{-1}. Each peak corresponded to specific vibrational modes of functional groups, enabling the identification of molecular components. These bands could be attributed to specific biomacromolecules, particularly proteins (amide I and II bands), lipids (ν(C–H) and ν(C═O) stretching vibrations) and water (ν(O–H) stretching and δ(H–O–H) bending vibrations), providing valuable molecular insights into the key components and their interactions within HPCs. Table 1 summarises the key FTIR peaks and their corresponding vibrational modes, identified based on characteristic assignments reported in the literature (Barth, 2007; Du et al., 2018).

For coconut oil, the characteristic absorption bands observed within the 2950–2800-cm^{-1} spectral range could be attributed to the asymmetric and symmetric stretching vibrations of methyl (–CH_3) and methylene (–CH_2) groups. A strong peak at 1744 cm^{-1} corresponded to the ν(C═O) stretching mode in ester functional groups, which was characteristic of triglycerides in lipids and represented total lipids. The bending vibrations of –CH_2 groups produced a peak at ~1465 cm^{-1}, while the band at 1160 cm^{-1} could be attributed to the ν(C–O–C) stretching in the –HC–O–(C═O) ester linkage (Gandhi et al., 2022). These key features helped analysing the lipid component in the HPC samples used in the present study at a molecular level.

Protein-associated absorption bands considerably helped identifying and characterising their secondary structures. The amide I band (1600–1700 cm^{-1}), which predominantly arose from the ν(C═O) stretching vibration, was highly sensitive to protein secondary structure owing to its dependence on the surrounding hydrogen bonding and

Table 1
Band assignment of FTIR absorption peaks typically found in most biological samples containing protein and lipid components (Barth, 2007; Bittante et al., 2022; Ørskov et al., 2023).

Wavenumber values (cm^{-1})	Functional groups	Component
3600–3200	ν(O–H)	Water/Hydroxyl groups
2950–2800	ν(C–H) from methyl (–CH_3) and methyl (–CH_2) groups of lipids	Lipids
1740[a]	ν(C═O) of esters from lipid triglycerides and fatty acids	Total lipids
1465[b]	$\delta_{scissor}(CH_2)$ from methylene (–CH_2) groups	Lipids
1700–1600	Amide I (ν(C═O) in peptide bonds)	Protein
1642–1610	β-sheet	
1650–1640	random coil	
1660–1650	α-helix	
1699–1660	β-turn	
1650–1640	δ(H–O–H)	Water
1570–1500	Amide II (δ(N–H) coupled with ν(C–N))	Proteins
1450	$BNQ1\delta_{as}(CH_3)$	Lipids
1400–1200	Amide III (δ(N–H) coupled with ν(C–N))	Protein
1160	ν_s(C–O–C) from esters	Lipids

Symbols used for vibrational modes: ν_{as} = asymmetric stretch; ν_s = symmetric stretch; δ_s = symmetric in-plane deformation (bend); δ_{as} = asymmetric in-plane deformation (bend); [a] Representative band for total lipids. [b] Sensitive to the orthorhombic-like to hexagonal packing transition of the –CH_2 groups in the phospholipid bilayers.

polypeptide backbone conformation. Characteristic wavenumber ranges for specific protein conformers included α-helices (1660–1650 cm^{-1}), random coil structures (1650–1640 cm^{-1}), β-sheets (1642–1610 cm^{-1}) and β-turns (1699–1660 cm^{-1}) (Hossain Brishti et al., 2021; Sadat & Joye, 2020). The amide II band (1550–1500 cm^{-1}), mainly attributed to δ(N–H) in-plane bending coupled with ν(C–N) stretching modes, contributed to protein structural analysis. These amide features played an important role in distinguishing plant-derived proteins from casein within complex food matrices.

Water exhibited strong characteristic absorption bands owing to its broad range of hydrogen interactions with other surrounding molecules within the food matrix. The broad ν(O–H) stretching band observed in the 3600–3200-cm^{-1} spectral range was associated with hydrogen bonding in water molecules and was highly sensitive to the physical state of water (e.g. free vs. bound water) and the surrounding molecular environment. A weaker δ(H–O–H) bending (scissoring) vibrational mode at ~1640 cm^{-1} often overlapped with the amide I band of proteins, potentially complicating spectral interpretation. These characteristic FTIR bands were the reference framework for analysing the single- and dual-protein hybrid cheese systems.

3.2. Spatial distribution of components and protein structure in single-protein systems

The FTIR chemical image of HPCs was generated by integrating specific absorption peaks corresponding to key chemical components, as outlined in the previous section. These included lipid-associated bands (2950–2800 and 1745 cm^{-1}), amide I (1700–1600 cm^{-1}) and water bands (3600–3200 cm^{-1}). Fig. 2 shows a representative chemical image of the RC100 sample. RC100 exhibited a homogeneous microstructure, with lipid droplets uniformly distributed within the casein network. The water signal overlapped within the casein matrix, suggesting a close spatial association between water and the casein matrix. This confirmed the amphipathic nature of casein, which possessed both hydrophilic and hydrophobic regions. The hydrophilic domains were capable of binding water, while the hydrophobic regions contributed to the stable incorporation of lipids into the protein matrix (Holt et al., 2013). This result is consistent with that of our previous confocal laser scanning microscopy (CLSM) study (Lu, Roy, et al., 2026).

However, the plant protein–based cheeses, such as MPI100 and HPI100, presented challenges for synchrotron macro ATR-FTIR measurements owing to their lower springiness and cohesiveness compared with the casein-based cheeses (Lu, Roy, et al., 2026). These physical limitations hindered optimal contact with the Ge ATR crystal, leading to partial loss of spectral information, a low signal-to-noise ratio and occasional sample movements during mapping. Representative images are provided in Supplementary Figure S1.

As obtaining a complete image of the plant-based cheese sample was challenging, protein and lipid spectra were successfully extracted based on peak intensities. These spectral data provided valuable insights into the chemical and functional group differences between plant proteins and casein. Fig. 3A shows the protein spectra generated for the RC100, MPI100 and HPI100 cheese samples, based on their integrated areas under the peaks as described in Section 2.2. The primary differences were observed in the amide I region; therefore, a second derivative analysis (Fig. 3B) and peak fitting were performed to further investigate the protein secondary structures of MPI (Fig. 3C), HPI (Fig. 3D) and RC (Fig. 3E) in the respective cheese samples. Notably, the water band at ~1640 cm^{-1} substantially overlapped with the protein random coil component in the amide I region and therefore could not be reliably separated during peak fitting.

The secondary structure analysis revealed distinct differences among the proteins. The β-sheet structures were observed to be the major protein conformer in the plant protein (1620 cm^{-1} in MPI100 and 1630 cm^{-1} in HPI100), while casein was predominated by random coil structures (1647 cm^{-1}). This finding was consistent with that of previous studies and suggested that plant proteins were more prone to aggregation, contributing to a more rigid cheese structure, while casein exhibited more disordered structures that could facilitate flexibility (Lu, Roy, et al., 2026).

Specifically, MPI exhibited a mixed secondary structure, consisting of α-helix (35%), β-sheet (48%), and β-turn structures (16%) (Fig. 3D). In comparison, HPI contained a lower proportion of α-helix (28%) but a higher content of β-sheets (50%) and β-turns (21%) (Fig. 3C). The increased β-turn content and reduced α-helical structure in HPI suggest a relatively less ordered secondary structure compared with MPI, which may influence its molecular conformational behaviour. RC was predominated by random coils (48%), along with the presence of a few β-sheets (23%) and β-turns (28%) (Fig. 3E). Notably, the β-sheet peak in MPI appeared at 1620 cm^{-1}, which was typically associated with intermolecular β-sheet formation involving stronger hydrogen bonding, suggesting a higher degree of protein aggregation (Sadat & Joye, 2020; Schestkowa et al., 2020). Comparatively, the β-sheet peak in HPI was more prominent at 1630 cm^{-1}, which was indicative of the association between intramolecular β-sheets and protein folding as well as stability, possibly reflecting a more compact and less aggregated structure (Eckhardt et al., 2024). The spectra of coconut oil were generated based on peak intensities obtained for RC100, MPI100 and HPI100. No marked differences were observed among them (Supplementary Figure S2).

3.3. Distinguish plant proteins and caseins in dual-protein cheese systems

Building on the identification of spectral features for individual components in single-protein systems, this section focuses on distinguishing plant proteins from casein within dual-protein hybrid cheeses. The analysis was performed to compare the performances of the two unsupervised classification approaches: HCA and k-means clustering. HCA group spectra were generated based on similarity without prior knowledge of sample composition, allowing for an exploratory assessment of the way different regions clustered together. Similarly, k-

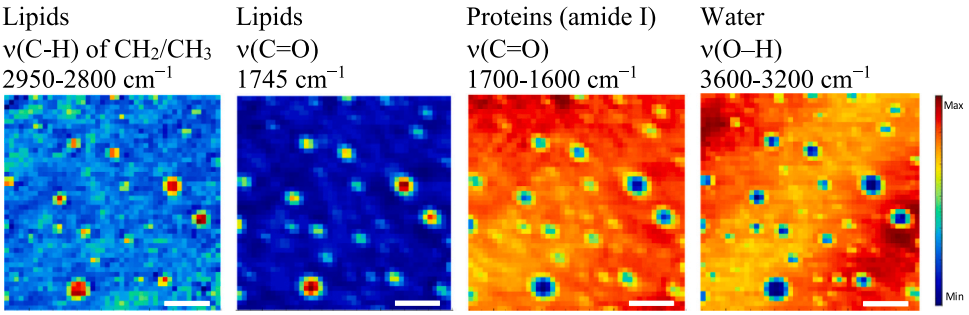

Fig. 2. A representative FTIR chemical image of the processed cheese formulated with 100% rennet casein (RC100). The distribution of lipids, proteins, and water was mapped using integrated areas under the peaks at 2950–2800 and 1745 cm^{-1}, 1700–1600 cm^{-1} and 3600–3200 cm^{-1}, respectively. Red and blue indicate high and low concentration, respectively, as shown by the colour intensity scale on the right. The scale bars are each 20 μm in length.

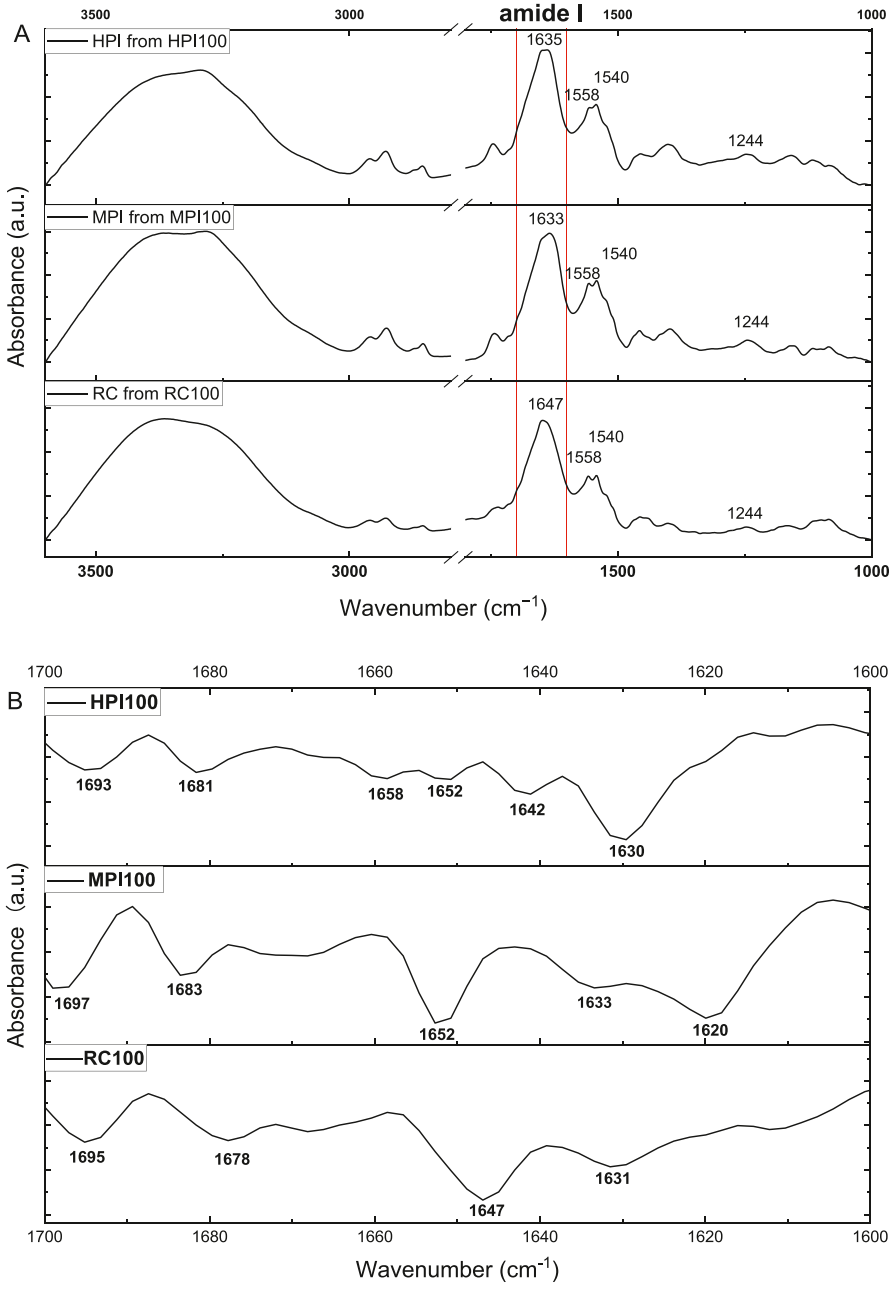

	α-helix (%)	Random coil (%)	β-sheet (%)	β-turn (%)
MPI100	35 ± 28	1 ± 2	48 ± 17	16 ± 12
HPI100	28 ± 10	1 ± 1	50 ± 6	21 ± 16
RC100	1	48 ± 15	23 ± 13	28 ± 2

Fig. 3. Average protein spectra of RC100, MPI100, and HPI100 cheese samples (A); corresponding second derivative spectra of the amide I region (B); and representative peak fitting of the amide I band for HPI (C), MPI (D), and RC (E). In the peak fitting, the black and yellow lines represent the experimental and final fitted spectra, respectively. The green, blue, red, and pink lines correspond to β-sheet, α-helix, random coil, and β-turn structures, respectively. RC100: cheese with 100% rennet casein; MPI100: cheese with 100% mung bean protein; HPI100: cheese with 100% hemp protein.

means clustering partitions spectra into distinct groups but uses an iterative centroid-based approach, which often produces more balanced cluster sizes.

Accordingly, the cluster maps of MPI50 and HPI50 were generated using HCA and k-means clustering (Fig. 4), respectively. Five clusters were identified in both HCA and k-means analyses, and the results were consistent between these two unsupervised methods. Notably, the edge regions consistently showed loss of spectral information owing to the highly collimated nature of the synchrotron-IR beam, highlighting the influence of imaging artefacts on the results. To further investigate the compositions of different clusters, small areas were selected for detailed analysis using HCA as an example (Figs. 5A and 5B).

The average second derivative spectra of MPI50 were extracted from the selected area of 23 × 23 μm^2 (Fig. 5A (1 and 4)). Clusters 1 (C1; green) and 2 (C2; blue) corresponded to protein-rich regions, which exhibited pronounced amide I bands, while cluster 4 (red) represented lipid-rich regions, which were characterised by strong ν(C–H) stretching vibrations and the ν(C═O) stretching mode of total lipids. Cluster 5 (orange) contained both proteins and lipids, forming a boundary surrounding the lipid-rich regions (Fig. 5A (4)). The PCA scatter plot, used for visualising cluster separation (Fig. 5A (2)), indicated that PC2 primarily distinguished C1 and C2, corresponding to the two protein types. Based on PC2 for ranking, the most discriminative features between mung bean protein and casein were observed to be the amide I band (particularly β-sheet structures), amide II band, lipid-related peaks and the absorption at ~1400 cm^{-1} . This absorption could be attributed to $\nu_s(COO^-)$ stretching modes associated with $\delta_s(CH_3)$ of fatty acids and amino acids (Dewantier et al., 2023; Movasaghi et al., 2008) (Fig. 5A (3)). The amide I and II regions, which are the key features that distinguish mung bean protein and casein, are presented in Fig. 5A (5) and (6), highlighting subtle differences in their peak positions and intensities. In the amide I region, C2 (blue) exhibited a more pronounced β-sheet signal (≈1618 cm^{-1}), while C1 (green) presented higher contributions from the random coil structures (≈1641 cm^{-1}). The amide II region displayed peaks at similar wavenumbers for both the clusters, with C2 exhibiting slightly higher intensity in the second derivative spectrum. Overall, these spectral patterns suggest that C1 is predominantly casein, while C2 is enriched with mung bean protein. Previous CLSM analysis further demonstrated that mung bean protein formed deflated spherical particles, while casein established the continuous network, with mung bean protein being a filler in MPI50 (Lu, Roy, et al., 2026), supporting this interpretation.

Similarly, the average second derivative spectra were extracted from a selected region of 38 × 42 μm^2 for HPI50 (Fig. 5B). Based on the spectral characteristics, it could be concluded that C1 (red) corresponds to lipid-rich domains, C2 (blue) and C3 (green) represent protein-rich regions and C5 (orange) exhibits mixed contributions from both protein and lipid (Fig. 5B (4)). PC2 indicated that the most discriminative features between hemp protein and casein were primarily associated with the amide II band, followed by the amide I band and lipid-related absorptions (Fig. 5B (3)). Within the amide I region, C2 and C3 displayed subtle differences in their secondary structure, particularly in the relative contributions of the α-helix (~1658 cm^{-1}) and β-turn (~1662 cm^{-1}) components. More pronounced distinctions were observed in the amide II region, where C2 was characterised by spectral features at ~1531, ~1548 and ~1567 cm^{-1}, while C3 was defined by peaks at ~1542 and ~1560 cm^{-1}. These variations reflect differences in backbone δ(N–H) bending and ν(C–N) stretching vibrations, which are known to be sensitive to hydrogen bonding and the electrostatic environment (Barth, 2007). Overall, the observed spectral patterns suggest that C2 was more consistent with hemp protein, while C3 aligned with casein. The increase in β-structure–associated signals in C2 was consistent with the aggregation tendency of hemp protein, while the spectral profile of C3 corresponded more closely to the flexible and random coil–rich structure of casein. These molecular-level distinctions provided direct evidence for the coexistence and differentiation of hemp protein and casein domains within the hybrid cheese matrix.

3.4. Protein–lipid and protein–protein interactions

Following distinguishing the two protein types within the dual-protein cheese matrix, this section examined the protein–lipid and protein–protein interactions in the mixed systems. C5 contained both protein and lipid peaks and was located adjacent to the lipid regions (Figs. 5A and 5B). In the scatter plot of the MPI50 samples (Fig. 5A (2)), C5 (orange) was positioned between C4 (lipid) and C1 (casein) but remained distant from C2 (mung bean protein). This spatial pattern indicated that coconut oil was more strongly co-located with casein than with mung bean protein, which could reflect higher hydrophobic compatibility between casein and lipid. By contrast, the scatter plot of HPI50 presented that C5 encompassed lipids, along with both hemp protein and casein, indicating the association of coconut oil with both types of protein. At the nanoscale, casein exhibits a highly amphiphilic network structure. In particular, β-casein readily adsorbs at the oil–water interface, forming a protective viscoelastic layer that prevents oil droplet coalescence and stabilizes lipid droplets (Zhai et al., 2011). In contrast, plant proteins are generally more rigid, with hydrophobic residues buried within the protein interior, leading to reduced interfacial interactions. They typically contain a higher proportion of β-sheet and fewer α-helix structures, exhibit more fibrillar conformations, and

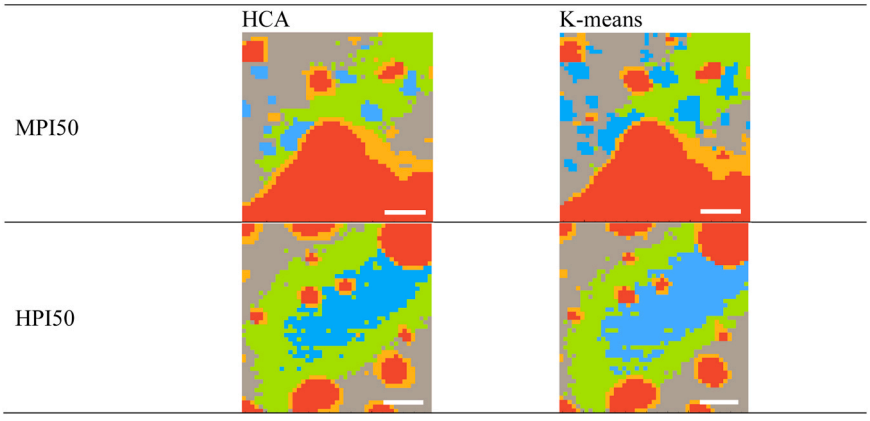

Fig. 4. Representative FTIR chemical images of MPI50 (top) and HPI50 (bottom) using hierarchical clustering (left) and k-means models (right). Rennet casein is shown in green, mung bean/hemp protein in blue, and lipid in red in MPI50 and HPI50. Different colors represent clusters identified through hierarchical clustering or K-means. Scale bars are 20 μm in length. MPI50: cheese formulated with 50% mung bean protein and 50% rennet casein. HPI50: cheese formulated with 50% hemp protein and 50% rennet casein.

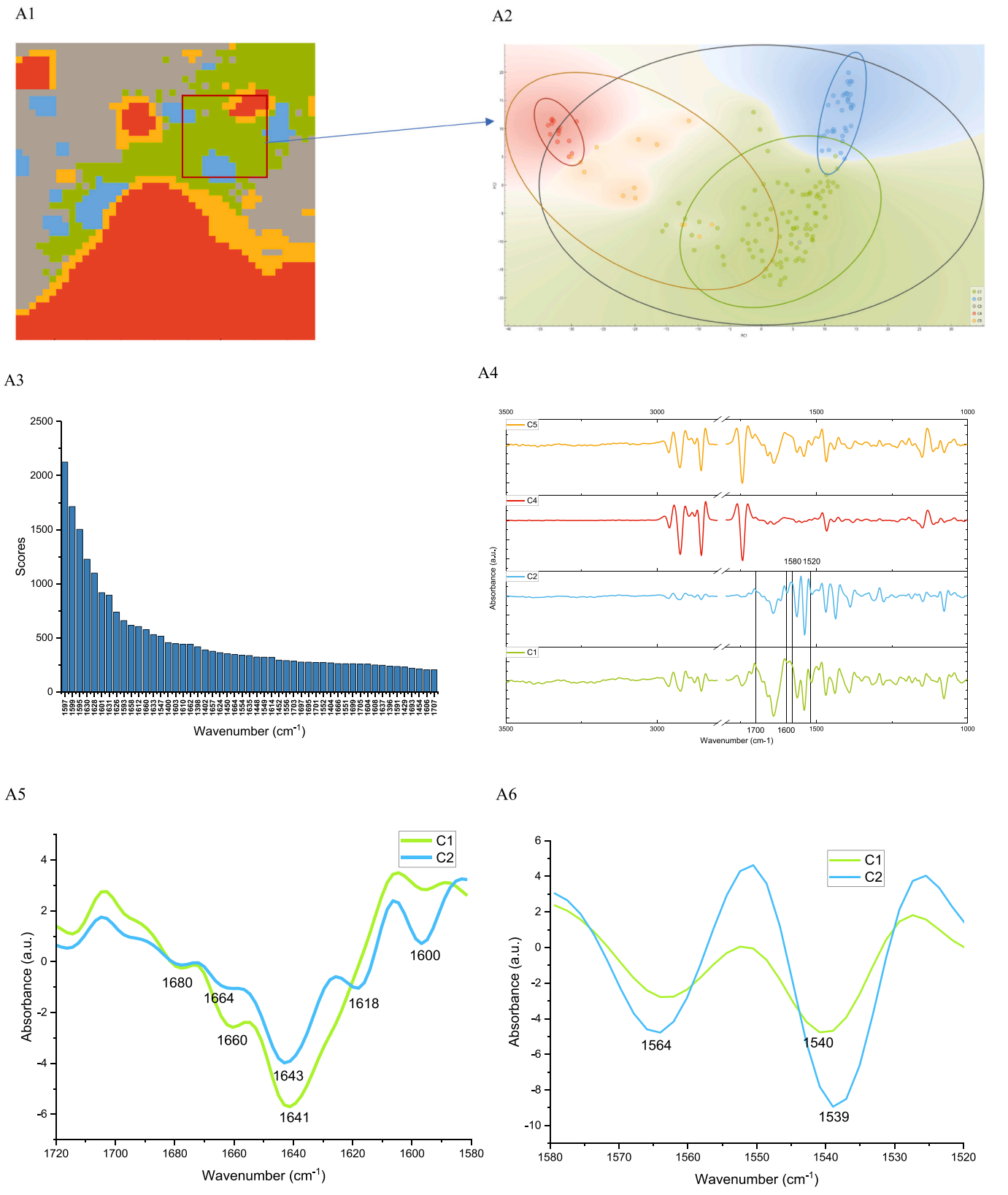

Fig. 5. FTIR chemical images of MPI50 (A) and HPI50 (B). For MPI50: (A1) hierarchical clustering image, the red box shows region of interest (A2) PCA scatter plot or spectra within region of interest from A1, (A3) ranking based on PC2, (A4) average second derivative spectra of clusters, (A5) amide I region, and (A6) amide II region. For HPI50: (B1) hierarchical clustering image, (B2) PCA scatter plot, (B3) ranking based on PC2, (B4) average second-derivative spectra of clusters, (B5) amide I region, and (B6) amide II region.

form interfacial films with lower modulus, making emulsions less stable under stress (Kim et al., 2020; Zhang et al., 2023). These findings were

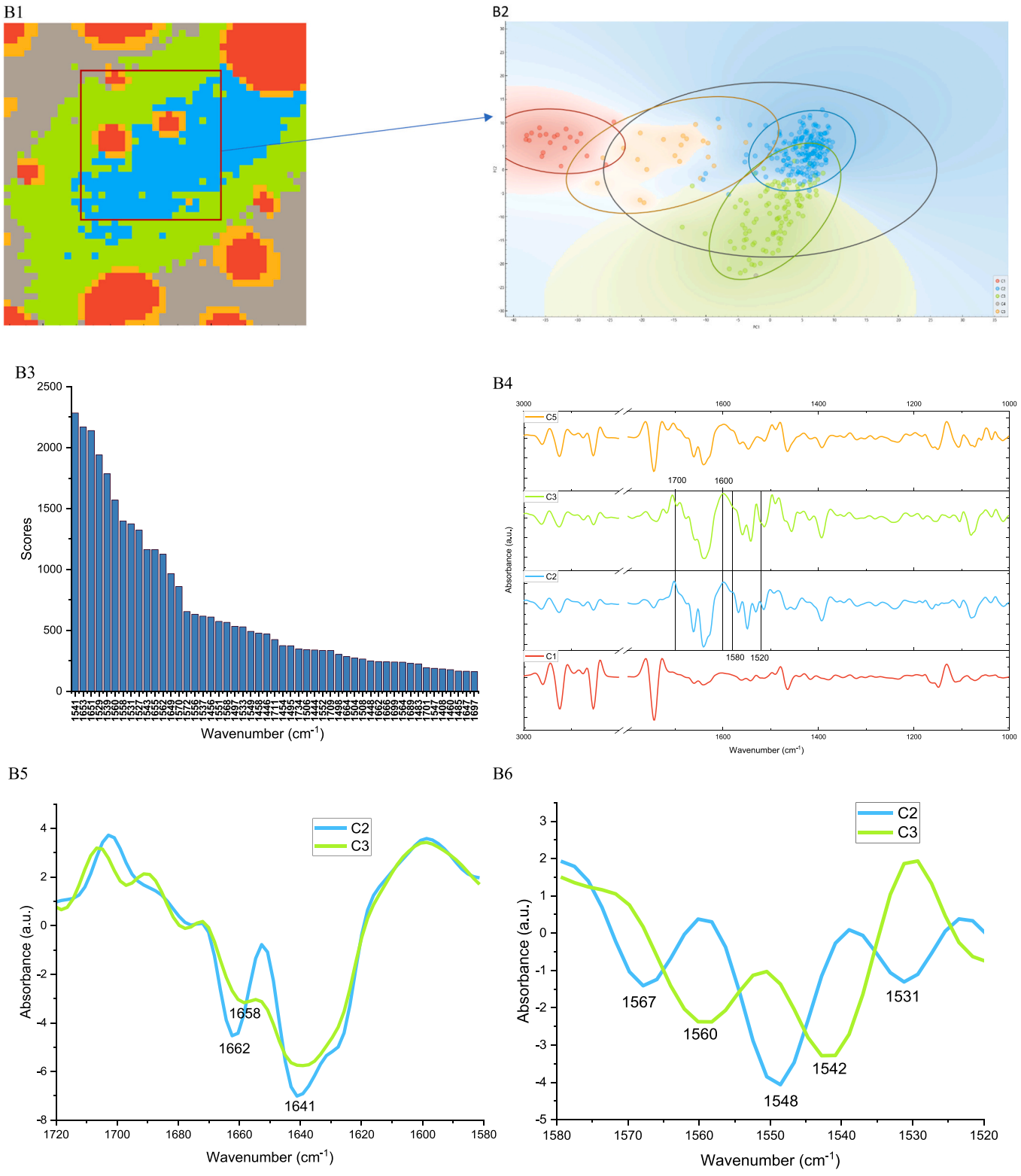

Fig. 5. (*continued*).

consistent with the TEM and CLSM observations (Lu, Roy, et al., 2026) and overall suggested that casein exhibited a strongest affinity towards coconut oil, followed by that of hemp protein, whereas mung bean protein exhibited a weaker association.

The spectra of MPI obtained from MPI100 and MPI50, HPI from HPI100 and HPI50 and RC from RC100, MPI50 and HPI50 were extracted to examine protein structural changes in the dual-protein systems (Fig. 6). In the ν(O–H) stretching region (3600–3000 cm^{-1}), the MPI spectrum obtained from MPI50 exhibited a broader ν(O–H) peak, with a higher wavenumber (~3375 cm^{-1}) than that of MPI100 (~3278 cm^{-1}) (Fig. 6A), indicating weaker hydrogen bonding. This suggests that water in MPI50 was more loosely bound and existed in a less structured hydration environment. The incorporation of casein likely disrupted the compact MPI network through physical interactions

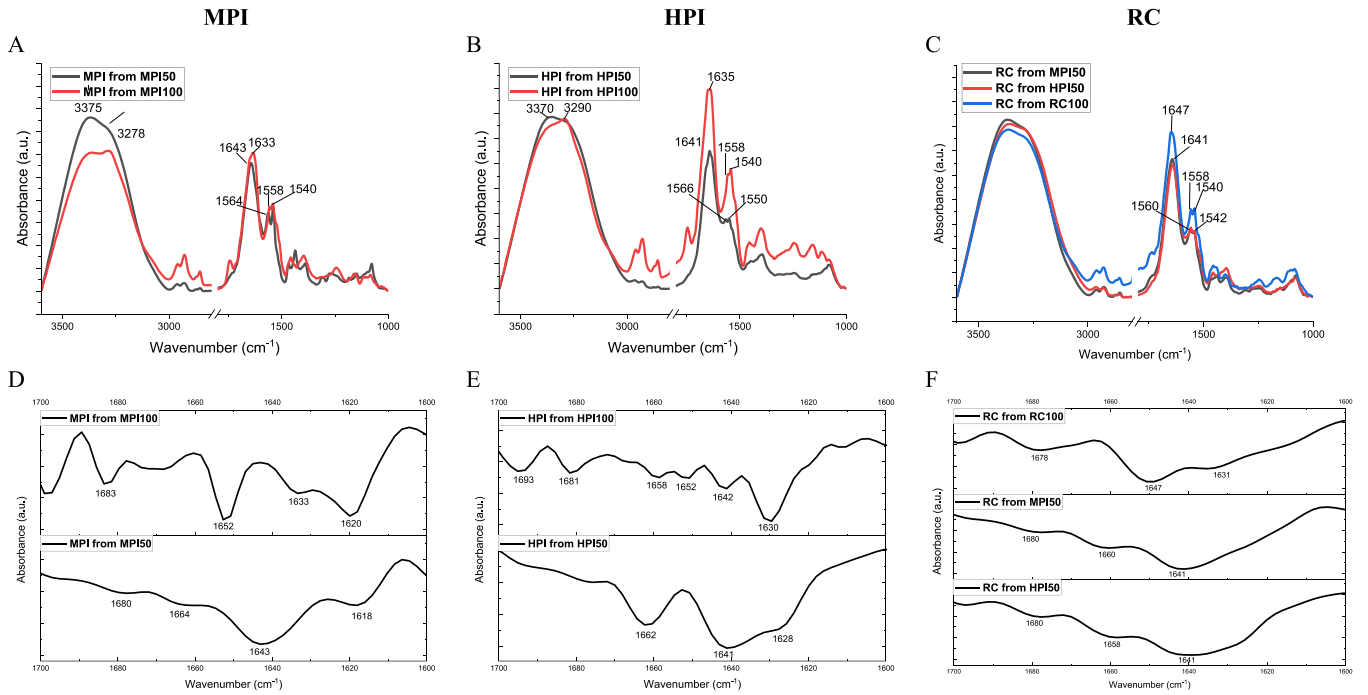

Fig. 6. FTIR spectra of (A) MPI (from MPI100 and MPI50), (B) HPI (from HPI100 and HPI50), and (C) RC (RC100, MPI50, HPI50) showing protein structural changes in dual-protein systems. Panels (D–F) present the corresponding second-derivative amide I spectra for MPI, HPI, and RC, respectively.

and competition for water, resulting in a more open and heterogeneous protein matrix in which water molecules were less constrained. In contrast, MPI100 formed denser aggregates with stronger water binding (Ushkalova et al., 2025). Consistent with this, Nascimento et al. (2024) reported that water-holding capacity is closely related to gel microstructure, with stronger and more compact gels retaining more water. Pure pea protein gels showed higher water-holding capacity than mixed pea–casein systems, which tend to form independent networks. The increased water mobility in the mixed system may be attributed to the presence of larger water-filled cavities of casein, whereas pure plant protein gels form a more compact network that restricts water movement (da Silva et al., 2025).

In the amide I region, the incorporation of casein decreased the β-sheet content of mung bean protein (~1633 cm^{-1}) while increasing the proportion of disordered protein structures (1643 cm^{-1}). Second derivative analysis (Fig. 6D) indicated decreases in α-helix and β-sheet structures with a concomitant increase in random coil contents. This suggested that casein disrupted β-sheet stacking and aggregation within the mung bean protein, resulting in a more disordered peptide environment. Furthermore, in the amide II region, the band at ~1540 cm^{-1} in MPI100 remained unchanged compared with that in MPI50, while the band at ~1558 cm^{-1} shifted to ~1564 cm^{-1}. This shift was indicative of changes in the local hydrogen-bonding environment around the peptide backbone, with higher wavenumbers reflecting weak N–H hydrogen bonding and more disordered local structure (Barth, 2007; Cobb et al., 2020). Although rheological and microstructural analyses showed that plant protein and casein did not co-aggregate during heating and instead formed independent networks at the micron scale (Lu, Roy, et al., 2026), the introduction of a second protein component nevertheless disrupted the aggregation behaviour and secondary structure of mung bean protein at smaller length scales. This effect can be attributed to structural frustration, whereby steric constraints and competition for water prevent optimal protein–protein packing, forcing local conformational rearrangements within the plant protein. Similar frustration effects have been reported in fibre and mixed gel systems, where local mismatches promote irregular void formation and weaken water retention (Liu et al., 2025). The small-angle X-ray scattering and nuclear magnetic resonance data have shown incorporation of 20% plant protein into casein gels (or vice versa) can induce structural changes, with gel properties governed by large-scale organization and pore size distribution rather than molecular composition alone (da Silva et al., 2025). An additional mechanism may contribute to the observed interactions between plant protein and casein in the mixed systems. Owing to the porous nature of the casein network, attractive interactions and partitioning behaviour may allow plant protein particles to partially penetrate the casein matrix, depending on their size. Smaller plant protein particles can occupy the pores within the casein network, simultaneously displacing water (Peixoto et al., 2015). This redistribution of water may reduce water-holding capacity and weaken protein–water hydrogen bonding, consistent with the higher ν(O–H) wavenumbers and the shifts in amide I and amide II bands observed by FTIR. Such size-dependent partitioning provides a mesoscale mechanism linking network architecture to local hydration and peptide bonding environments.

Similarly, the addition of casein in HPI50 produced a more heterogeneous spectrum, and the dominant ν(O–H) absorption peak shifted to a higher wavenumber (~3370 cm^{-1}) than that observed for HPI100 (~3290 cm^{-1}). This blue shift indicated that the mixed system resulted in a higher proportion of loosely hydrogen-bonded water, suggesting a less compact network structure than that of the pure hemp protein matrix. This effect occurred owing to the chaperone-like activity of casein, which could inhibit protein self-aggregation (Chuang et al., 2019). In addition, casein could compete with HPI for forming hydrogen bonds with water and protein side chains, further limiting HPI–HPI interactions. This was accompanied by a decrease in β-sheet protein (~1633 cm^{-1}) and an increase in disordered (~1641 cm^{-1}) and β-turn (1662 cm^{-1}) structures (Figs. 6B and 6E), consistent with a less aggregated and more flexible protein network. In the amide II region (mainly δ(N–H) and ν(C–N) modes), the bands at ~1540 and ~1558 cm^{-1} in HPI100 shifted to ~1550 and ~ 1566 cm^{-1}, respectively. These blue shifts towards the high energy range reflect alterations in the local hydrogen-bonding environment around the peptide backbone. Similar hydrogen bond–mediated shifts have been reported for starch–casein systems (Sun et al., 2016), highlighting the role of hydrogen bonding in modulating protein–matrix interactions. While comparing the RC

spectra from RC100, MPI50 and HPI50, no notable changes were observed (Fig. 6C). However, analysis of the second derivative spectra indicated minor differences in the RC component between MPI50, HPI50 and RC100. Specifically, the peaks at ~1640 cm^{-1} were broader in the mixed-protein systems and exhibited a small shoulder corresponding to α-helical protein structures. These observations suggest that the presence of casein better perturbs the structural organisation of plant proteins than vice versa.

Overall, in the mixed systems, despite the formation of independent protein networks at the micron scale, both networks occupy the same physical space and aggregate simultaneously. Competition for water and local hydrogen-bond rearrangements generate intermediary-scale structural frustration, which disrupts the native folding and aggregation pathways of each protein. These effects are sufficient to modify the vibrational environments of O–H, amide I, and amide II groups, explaining the observed spectral shifts in the mixed systems.

3.5. Complementary insights into Raman and S-FTIR results

FTIR and Raman spectroscopies are complementary techniques, as polar groups produce strong IR absorptions, while nonpolar groups exhibit strong Raman scattering. Raman microspectroscopy was previously employed for characterising HPCs, identifying protein types, lipids and additives in hybrid cheese as well as for distinguishing the interactions between MPI–casein and HPI–casein. HPI increased structural disorder and facilitated disulphide bond rearrangements, while MPI enhanced protein domain separation due to stronger aggregation and higher β-sheet content (Lu, McGoverin, et al., 2026; Lu, Roy, et al., 2026). Herein, the molecular information obtained by conducting S-FTIR and Raman microspectroscopies was observed to be correlated; their complementary insights are summarised in Table 2.

Protein analysis in high-moisture systems was particularly challenging for FTIR spectroscopy, as the intense δ(H–O–H) bending vibration of water overlapped with the amide I region, complicating analysis of the secondary protein structure (Miller & Dumas, 2010; Sadat & Joye, 2020). Although FTIR spectroscopy is the gold standard for analysing protein secondary structure owing to its strong amide I/II signals and extensive spectral databases, its application in hydrated materials remains limited. Alternatively, Raman spectroscopy is far less affected by water interference, as its scattering intensity depends on the changes in molecular polarizability, with strongly polar water molecules contributing only weak Raman signals (Larkin, 2018). In addition, Raman spectroscopy is particularly sensitive to disulphide bonds and aromatic residues, while confocal mapping correlates structural and microstructural features. As the hybrid cheese examined in this study contained ~40% moisture (Lu, Roy, et al., 2026), Raman spectroscopy became a relatively robust tool for examining protein structural changes. At the same time, FTIR spectroscopy was a valuable method used for cross-validation and providing complementary insights. The FTIR and Raman spectroscopy results were consistent with the previous reports on hemp globulin–casein interactions. For example, Chuang et al. (2019) showed that casein exerted a chaperone-like effect, inhibiting hemp globulin aggregation and improving colloidal stability. Meanwhile, Chuang et al. (2021) that pH-cycling promoted HG–SC nanoparticle formation mainly via hydrogen bonding and disulfide interactions. Similarly, our FTIR analysis suggested that casein suppressed β-sheet formation in hemp protein (limiting aggregation) through hydrogen bonding, while the Raman analysis results indicated disulphide bond rearrangement and increased structural disorder in hybrid cheese (Lu, McGoverin, et al., 2026). These complementary findings indicate that HPI–casein creates a flexible, dynamic protein network that supports enhanced meltability and aligning with lower G′ values and a more deformable, energy-dissipating network. By contrast, the stronger aggregation and higher β-sheet content of MPI result in a rigid, segmented microstructure with pronounced protein domain separation, elevated G′, and reduced network connectivity, which is consistent with decreased meltability and stretchability (Lu, Roy, et al., 2026). These structural differences highlight how protein secondary structure and molecular interactions directly influence the macroscopic texture and functional properties of hybrid cheeses.

Dewantier et al. (2023) applied FTIR and Raman spectroscopy to classify cheddar cheeses by maturity, with the amide I and II bands driving FTIR classification and lipid-associated bands dominating in Raman spectra. Ørskov et al. (2023) used the same techniques to assess the microstructural composition and interactions in imitation cheese containing casein, lipids and modified starches. Although these methods successfully identified the components, they failed to resolve the specific interaction types, likely owing to limited resolution. This limitation underscored the need for more advanced analytical approaches, such as high-resolution S-FTIR, to unravel the detailed interactions within the complex food matrix.

Sadat and Joye (2020) compared the results of FTIR and FT-Raman spectroscopy for analysing the secondary structure of four globular proteins in aqueous solution and hydrated zein and gluten, demonstrating that water removal was essential for obtaining FTIR spectra. After correction, both FT-Raman and FTIR spectra were well defined with comparable secondary structure estimations. However, herein, water removal was not performed to preserve the native hydration environment of the proteins. Moreover, as the interaction of protein with water could slightly shift the H_2O bending signal (Zuber et al., 1992), there remained a risk of the development of subtraction artefacts. To leverage the combined strengths of FTIR and Raman spectroscopies, a multimodal approach was developed by combining both the techniques; this integration enabled a more thorough and nuanced exploration of chemical structures (Jurowski et al., 2024). This became a powerful tool for conducting studies on complex food matrices in future.

Table 2
Complementary insights of confocal Raman microscopy and S-FTIR for protein structure analysis in HPCs.

Spectroscopic Feature	Confocal Raman Microscopy (1800–200 cm^{-1})	Synchrotron FTIR (4000–1000 cm^{-1})
Sample preparation	Simple	Simple
Amide I (1700–1600 cm^{-1})	Good sensitivity; less water interference; suitable for secondary structure deconvolution	Strong sensitivity, but water absorbance overlaps in amide I (1650–1640 cm^{-1}), complicating analysis in HPCs
Amide II (1570–1500 cm^{-1})	Weaker signal	Stronger than Raman spectroscopy
Amide III (1400–1200 cm^{-1})	Detectable, complementary to Amide I	Weak in HPCs
I_{850}/I_{830} ratio, Tyr environment)	Yes – informative on protein–water interactions	No
S–S stretch (550–500 cm^{-1})	Yes – useful for monitoring disulfide bonds and conformational stability	Not accessible
Phospholipids (1001 cm^{-1})	Yes – can detect	Limited – less specific
Water interference	Minimal	Strong δ(H–O–H) bending overlaps with amide I
Spatial resolution	High (~1 μm)	Good with synchrotron-IR beam (3.2 μm)
Suitability for HPCs (~40% moisture)	Highly suitable – less spectral distortion from water, can resolve protein/lipid domains in situ	Challenging – strong water absorbance makes secondary structure analysis less reliable

4. Conclusions

This study used high-resolution S-FTIR microspectroscopy to map the spatial distribution of the key biomacromolecules in processed hybrid cheeses and to differentiate plant proteins from casein via unsupervised multivariate analysis. Although both HCA and k-means

clustering produced broadly similar spatial patterns, HCA generated more stable and structurally meaningful clusters. Therefore, subsequent analyses were based on HCA results. This technique offered insights into intermolecular interactions, such as protein–protein and protein–lipid interactions. Overall, the S-FTIR results were complementary to those obtained from Raman spectroscopy, reinforcing the observations across both the techniques.

In the hemp protein–casein cheeses, the S-FTIR results suggested that the interactions between hemp protein and casein were likely mediated by hydrogen bonding and Raman spectroscopy offered a complementary insight into the arrangement of disulfide bonds. The amide II region emerged as the key spectral feature that distinguished these two protein types. Alternatively, for mung bean protein–casein cheeses, the amide I region played the dominant role in differentiating casein from mung bean protein. Increasing the proportion of casein in these mixtures reduced both MPI and HPI aggregation and weakened N–H hydrogen bonding, indicating that water was less strongly bound and that the protein network was more flexible.

Regarding lipid distribution, S-FTIR analysis indicated that coconut oil was preferentially associated with casein rather than with plant proteins. Overall, these findings highlighted the complementary nature of S-FTIR and Raman spectroscopies in resolving both compositional differences and molecular interactions within hybrid cheese matrices.

Funding

This research work was supported by the Riddet Institute Centre of Research Excellence (CoRE), funded by the New Zealand Tertiary Education Commission. This research was supported by the New Zealand Synchrotron Group Ltd, which provides funding for New Zealand researchers and students to access the Australian Synchrotron.

Declaration of Competing Interest

The authors declare that they have no known competing financial interests or personal relationships that could have appeared to influence the work reported in this paper.

Acknowledgments

The synchrotron macro ATR-FTIR experiment was undertaken at the Infrared Microspectroscopy (IRM) beamline at the Australian Synchrotron, part of ANSTO, via merit-based beamtime proposal (ID. M22940) in February 2025.

Appendix A. Supporting information

Supplementary data associated with this article can be found in the online version at doi:10.1016/j.foostr.2026.100511.

Data Availability

Data will be made available on request.

References

Barth, A. (2007). Infrared spectroscopy of proteins. *Biochimica et Biophysica Acta (BBA) - Bioenergetics, 1767*(9), 1073–1101. https://doi.org/10.1016/j.bbabio.2007.06.004

Bittante, G., Patel, N., Cecchinato, A., & Berzaghi, P. (2022). Invited review: A comprehensive review of visible and near-infrared spectroscopy for predicting the chemical composition of cheese. *Journal of Dairy Science, 105*(3), 1817–1836. https://doi.org/10.3168/jds.2021-20640

Chuang, C.-C., Wegrzyn, T. F., Anema, S. G., & Loveday, S. M. (2019). Hemp globulin heat aggregation is inhibited by the chaperone-like action of caseins. *Food Hydrocolloids*.

Chuang, C. C., Ye, A., Anema, S. G., & Loveday, S. M. (2021). Hemp globulin forms colloidal nanocomplexes with sodium caseinate during pH-cycling. *Food Research International, 150*(Pt B), Article 110810. https://doi.org/10.1016/j.foodres.2021.110810

Cobb, J. S., Zai-Rose, V., Correia, J. J., & Janorkar, A. V. (2020). FT-IR spectroscopic analysis of the secondary structures present during the desiccation induced aggregation of elastin-like polypeptide on silica. *ACS Omega, 5*(14), 8403–8413. https://doi.org/10.1021/acsomega.0c00271

Dewantier, G. R., Torley, P. J., & Blanch, E. W. (2023). Identifying chemical differences in cheddar cheese based on maturity level and manufacturer using vibrational spectroscopy and chemometrics. *Molecules, 28*(24), 8051. ⟨https://www.mdpi.com/1420-3049/28/24/8051⟩.

Du, M., Xie, J., Gong, B., Xu, X., Tang, W., Li, X., Li, C., & Xie, M. (2018). Extraction, physicochemical characteristics and functional properties of Mung bean protein. *Food Hydrocolloids, 76*, 131–140. https://doi.org/10.1016/j.foodhyd.2017.01.003

Eckhardt, L., Bu, F., Franczyk, A., Michaels, T., & Ismail, B. P. (2024). Hemp (Cannabis sativa L.) protein: Impact of extraction method and cultivar on structure, function, and nutritional quality. *Current Research in Food Science, 8*, Article 100746. https://doi.org/10.1016/j.crfs.2024.100746

Fellows, A. P., Casford, M. T. L., & Davies, P. B. (2020). Spectral analysis and deconvolution of the amide I band of proteins presenting with high-frequency noise and baseline shifts. *Applied Spectroscopy, 74*(5), 597–615. https://doi.org/10.1177/0003702819898536

Gandhi, K., Sharma, R., Seth, R., & Mann, B. (2022). Detection of coconut oil in ghee using ATR-FTIR and chemometrics. *Applied Food Research, 2*(1), Article 100035. https://doi.org/10.1016/j.afres.2021.100035

Holt, C., Carver, J. A., Ecroyd, H., & Thorn, D. C. (2013). Invited review: Caseins and the casein micelle: Their biological functions, structures, and behavior in foods1. *Journal of Dairy Science, 96*(10), 6127–6146. https://doi.org/10.3168/jds.2013-6831

Hossain Brishti, F., Chay, S. Y., Muhammad, K., Rashedi Ismail-Fitry, M., Zarei, M., Karthikeyan, S., Caballero-Briones, F., & Saari, N. (2021). Structural and rheological changes of texturized mung bean protein induced by feed moisture during extrusion. *Food Chemistry, 344*, Article 128643. https://doi.org/10.1016/j.foodchem.2020.128643

Jurowski, K., Noga, M., Kobylarz, D., Niżnik, Ł., & Krośniak, A. (2024). Multimodal imaging using raman spectroscopy and FTIR in a single analytical instrument with a microscope (Infrared Raman Microscopy AIRsight, Shimadzu): Opportunities and applications. *International Journal of Molecular Sciences, 25*(13). https://doi.org/10.3390/ijms25136884

Kim, W., Wang, Y., & Selomulya, C. (2020). Dairy and plant proteins as natural food emulsifiers. *Trends in Food Science & Technology, 105*, 261–272. https://doi.org/10.1016/j.tifs.2020.09.012

Kim, W., Wang, Y., Vongsvivut, J., Ye, Q., & Selomulya, C. (2023). On surface composition and stability of β-carotene microcapsules comprising pea/whey protein complexes by synchrotron-FTIR microspectroscopy. *Food Chemistry, 426*, Article 136565. https://doi.org/10.1016/j.foodchem.2023.136565

Koca, N., Rodriguez-Saona, L. E., Harper, W. J., & Alvarez, V. B. (2007). Application of Fourier transform infrared spectroscopy for monitoring short-chain free fatty acids in Swiss cheese. *Journal of Dairy Science, 90*(8), 3596–3603. https://doi.org/10.3168/jds.2007-0063

Larkin, P. J. (2018). *Infrared and Raman Spectroscopy (Second Edition)*. Elsevier. https://doi.org/10.1016/B978-0-12-804162-8.00001-X

Liu, Y., Wei, L., Zhang, J., Cao, Z., Yang, G., Zhou, C., Li, Y., & Wang, W. (2025). Tunable techno-functional properties of pea protein gel through microbial transglutaminase synergize pea inner fiber with varying particle sizes and volumetric ratio. *Food Research International, 221*, Article 117374. https://doi.org/10.1016/j.foodres.2025.117374

Lu, D., McGoverin, C., Roy, D., Acevedo-Fani, A., Singh, H., Waterland, M., Zheng, Y., & Ye, A. (2026). Distinguishing plant and milk proteins and their interactions in hybrid cheese using confocal Raman microscopy with machine learning. *Food Chemistry, 498*, Article 147102. https://doi.org/10.1016/j.foodchem.2025.147102

Lu, D., Roy, D., Acevedo-Fani, A., Singh, H., Waterland, M., & Ye, A. (2026). Physical properties and microstructure of hybrid processed cheeses formulated with plant protein and milk protein ingredients. *Food Hydrocolloids, 170*, Article 111688. https://doi.org/10.1016/j.foodhyd.2025.111688

Lu, D., Roy, D., Acevedo-Fani, A., Singh, H., & Ye, A. (2025). Investigation of various plant protein ingredients for processed cheese analogues: physical properties and microstructure compared with milk proteins. *International Journal of Food Science and Technology, 60*(1). https://doi.org/10.1093/ijfood/vvae018

Margolies, B. J., & Barbano, D. M. (2018). Determination of fat, protein, moisture, and salt content of Cheddar cheese using mid-infrared transmittance spectroscopy. *Journal of Dairy Science, 101*(2), 924–933. https://doi.org/10.3168/jds.2017-13431

Miller, L. M., & Dumas, P. (2010). From structure to cellular mechanism with infrared microspectroscopy. *Current Opinion in Structure Biology, 20*(5), 649–656. https://doi.org/10.1016/j.sbi.2010.07.007

Movasaghi, Z., Rehman, S., & ur Rehman, D. I. (2008). Fourier Transform Infrared (FTIR) Spectroscopy of Biological Tissues. *Applied Spectroscopy Reviews, 43*(2), 134–179. https://doi.org/10.1080/05704920701829043

Nascimento, L. G. L., da Silva, R. R., Odelli, D., Doumert, B., Martins, E., Casanova, F., Marie, R., Carvalho, A. F., Delaplace, G., & de Sá Peixoto Junior, P. P. (2024). Acid gelation of high-concentrated casein micelles and pea proteins mixed systems. *Food Research International, 196*, Article 114982. https://doi.org/10.1016/j.foodres.2024.114982

Ong, L., Pax, A. P., Ong, A., Vongsvivut, J., Tobin, M. J., Kentish, S. E., & Gras, S. L. (2020). The effect of pH on the fat and protein within cream cheese and their influence on textural and rheological properties. *Food Chemistry, 332*, Article 127327. https://doi.org/10.1016/j.foodchem.2020.127327

Ørskov, K. E., Christensen, L. B., Wiking, L., Hannibal, T., & Hammershøj, M. (2023). Detecting interactions between starch and casein in imitation cheese by FTIR and

Raman spectroscopy. *Food Chemistry Advances, 2*, Article 100322. https://doi.org/10.1016/j.focha.2023.100322

Pax, A. P., Ong, L., Pax, R. A., Vongsvivut, J., Tobin, M. J., Kentish, S. E., & Gras, S. L. (2023). Industrial freezing and tempering for optimal functional properties in thawed Mozzarella cheese. *Food Chemistry, 405*, Article 134933. https://doi.org/10.1016/j.foodchem.2022.134933

Pax, A. P., Ong, L., Vongsvivut, J., Tobin, M. J., Kentish, S. E., & Gras, S. L. (2019). The characterisation of Mozzarella cheese microstructure using high resolution synchrotron transmission and ATR-FTIR microspectroscopy. *Food Chemistry, 291*, 214–222. https://doi.org/10.1016/j.foodchem.2019.04.016

Peixoto, P. D., Bouchoux, A., Huet, S., Madec, M. N., Thomas, D., Floury, J., & Gésan-Guiziou, G. (2015). Diffusion and partitioning of macromolecules in casein microgels: evidence for size-dependent attractive interactions in a dense protein system. *Langmuir, 31*(5), 1755–1765. https://doi.org/10.1021/la503657u

Sadat, A., & Joye, I. (2020). Peak Fitting Applied to Fourier Transform Infrared and Raman Spectroscopic Analysis of Proteins. *Applied Sciences, 10*(17), 5918. https://doi.org/10.3390/app10175918

Saji, R., Ramani, A., Gandhi, K., Seth, R., & Sharma, R. (2024). Application of FTIR spectroscopy in dairy products: A systematic review. *Food and Humanity, 2*, Article 100239. https://doi.org/10.1016/j.foohum.2024.100239

Schestkowa, H., Drusch, S., & Wagemans, A. M. (2020). FTIR analysis of β-lactoglobulin at the oil/water-interface. *Food Chemistry, 302*, Article 125349. https://doi.org/10.1016/j.foodchem.2019.125349

Silva, D. M., Dos Reis, L. G., Tobin, M. J., Vongsvivut, J., Traini, D., & Sencadas, V. (2021). Co-delivery of inhalable therapies: Controlling active ingredients spatial distribution and temporal release. *Materials Science and Engineering, 122*, Article 111831. https://doi.org/10.1016/j.msec.2020.111831

da Silva, R. R., Odelli, D., Descamps, A., Scudeller, L. A., Doumert, B., Perez, J., Delaplace, G., de Carvalho, A. F., & de Sá Peixoto Junior, P. P. (2025). Multi-scale organization and rheology of casein and pea protein mixed hydrogels formed by acidification: Effects of ratio and temperature. *Food Research International, 209*, Article 116242. https://doi.org/10.1016/j.foodres.2025.116242

Sun, N.-x, Liang, Y., Yu, B., Tan, C.-p, & Cui, B. (2016). Interaction of starch and casein. *Food Hydrocolloids, 60*, 572–579. https://doi.org/10.1016/j.foodhyd.2016.04.029

Tang, Q., Roos, Y. H., & Miao, S. (2023). Plant Protein versus Dairy Proteins: A pH-Dependency Investigation on Their Structure and Functional Properties. *Foods, 12*(2), 368. ⟨https://www.mdpi.com/2304-8158/12/2/368⟩.

Timilsena, Y. P., Vongsvivut, J., Tobin, M. J., Adhikari, R., Barrow, C., & Adhikari, B. (2019). Investigation of oil distribution in spray-dried chia seed oil microcapsules using synchrotron-FTIR microspectroscopy. *Food Chemistry, 275*, 457–466. https://doi.org/10.1016/j.foodchem.2018.09.043

Toplak, M., Read, S., Sandt, C., & Borondics, F. (2021). Quasar: Easy Machine Learning for Biospectroscopy. *Cells, 10*, 2300. https://doi.org/10.3390/cells10092300

Ushkalova, A. A., Zhao, R., Gu, Y., Wang, C., & Zhang, T. (2025). Partially substituting cheese base with plant proteins to produce processed cheese: Textural, rheological, microstructural and sensory properties. *Journal of Dairy Science, 108*(5), 4638–4658. https://doi.org/10.3168/jds.2025-26296

Vongsvivut, J., Pérez-Guaita, D., Wood, B. R., Heraud, P., Khambatta, K., Hartnell, D., Hackett, M. J., & Tobin, M. J. (2019). Synchrotron macro ATR-FTIR microspectroscopy for high-resolution chemical mapping of single cells [10.1039/C8AN01543K] *Analyst, 144*(10), 3226–3238. https://doi.org/10.1039/C8AN01543K.

Yiu, C. C.-Y., Kim, W., Gunawan, I. C., Vongsvivut, J., Wang, Y., & Selomulya, C. (2026). A dual polysaccharide and plant protein system for cheese analog with enhanced meltability and texture. *Food Hydrocolloids, 171*, Article 111850. https://doi.org/10.1016/j.foodhyd.2025.111850

Zhai, J., Waddington, L., Wooster, T. J., Aguilar, M.-I., & Boyd, B. J. (2011). Revisiting β-Casein as a Stabilizer for Lipid Liquid Crystalline Nanostructured Particles. *Langmuir, 27*(24), 14757–14766. https://doi.org/10.1021/la203061f

Zhang, D., Jiang, K., Luo, H., Zhao, X., Yu, P., & Gan, Y. (2024). Replacing animal proteins with plant proteins: Is this a way to improve quality and functional properties of hybrid cheeses and cheese analogs? *Comprehensive Reviews in Food Science and Food Safety, 23*(1), Article e13262. https://doi.org/10.1111/1541-4337.13262

Zhang, X., Wang, Q., Liu, Z., Zhi, L., Jiao, B., Hu, H., Ma, X., Agyei, D., & Shi, A. (2023). Plant protein-based emulsifiers: Mechanisms, techniques for emulsification enhancement and applications. *Food Hydrocolloids, 144*, Article 109008. https://doi.org/10.1016/j.foodhyd.2023.109008

Zuber, G., Prestrelski, S. J., & Benedek, K. (1992). Application of Fourier transform infrared spectroscopy to studies of aqueous protein solutions. *Analytical Biochemistry, 207*(1), 150–156. https://doi.org/10.1016/0003-2697(92)90516-a